ELSEVIER
International Journal of Solids and Structures 41 (2004) 1581–1604
INTERNATIONAL JOURNAL OF SOLIDS and STRUCTURES
www.elsevier.com/locate/ijsolstr

Transition from progressive buckling to global bending of circular shells under axial impact—Part II: Theoretical analysis

D. Karagiozova [a,*], Marcílio Alves [b,*]

[a] *Institute of Mechanics, Bulgarian Academy of Sciences, Acad. G. Bonchev St., Block 4, Sofia 1113, Bulgaria*
[b] *Department of Mechatronics and Mechanical Systems Engineering, University of São Paulo, CP 8174, São Paulo 05508-900, Brazil*

Received 28 July 2003; received in revised form 24 September 2003

Abstract

This is the second paper of a two-part paper investigating the complex phenomenon of the dynamic transition from progressive buckling to global bending collapse of a long circular cylindrical shell subjected to an axial impact. The paper focuses on the theoretical analysis of the phenomenon. The two-phase concept for the deformation of 'Type II' structures is employed to explore the influence of the loading parameters and the material and geometrical characteristics of a shell on the critical length that marks the transition between the two collapse modes. Simple models for the initial compressive phase in the case of global bending and for the development of a single axisymmetric wrinkle in a circular shell, are used to analyse some numerical results presented in Part I of this study [International Journal of Solids and Structures 41 (2004) 1565].

Keywords: Progressive buckling; Global bending; Axial impact; Simple models; Elastic–plastic circular shells

---

1. Introduction

The experiments on the dynamic buckling transition of relatively long circular tubes discussed in Part I (Karagiozova and Alves, 2004) show that, in contrast to the static response reported by Andrews et al. (1983) and Abramowicz and Jones (1997), tubes with identical characteristics $2R/h$ and $L/2R$ can respond either by progressive buckling or global bending when subjected to axial impact loads depending on the initial velocity. The numerical simulations of the dynamic buckling transition in Part I (Karagiozova and Alves, 2004) reveal that a variation of the material properties can alter the collapse mode of circular tubes when identical dynamic loads are applied. It is evident that the phenomenon is influenced by various factors. Therefore, the objective of this study is to explore via a theoretical analysis the influence of the characteristic parameters on the dynamic buckling transition.

---

[*] Corresponding authors. Tel.: +55-11-8185560; fax: +55-11-30615560.
E-mail addresses: d.karagiozova@imbm.bas.bg (D. Karagiozova), maralves@usp.br (M. Alves).

0020-7683/$ - see front matter
doi:10.1016/j.ijsolstr.2003.10.006

Nomenclature

A	cross-section area of a shell
E, E_h, E_r	the Young's modulus, hardening and reduced modulus, respectively
F^s, F^θ	axial and circumferential forces in a shell, respectively
F^c	radial force in the model in Fig. 9
D, q	material constants, Eq. (37)
G	impact mass
G_1	impact mass per unit circumferential length
L	length of a shell
M	mass of a shell
R	radius of a shell
T_0, T_b, T_c	initial kinetic energy, bending and compression energy, respectively
V	velocity
V_0	initial impact velocity
V^*	initial velocity of the proximal end of the model in Fig. 6 at the end of the compression phase
c, c_1	bending rigidity coefficients, Eqs. (9) and (2), respectively
h	thickness of a shell
l	$1.34\sqrt{Rh}$, length of a link (Fig. 9)
m	mass per unit length (Fig. 6)
m^*	mass per unit circumferential length of a single wrinkle (Fig. 9)
n_t	$(2n_t+1)$, number of integration points across the shell thickness (Eq. (30)–(34))
t	time
t^*	time at the end of the compression phase
u	axial displacement of a shell (Fig. 6)
w	lateral displacement
w_0	initial lateral displacement (Figs. 6 and 9)
x, z	axial and through the thickness coordinates of a shell, respectively
Δ	axial compression (overall reduction of the shell length)
ε_e, ε_x, ε_θ	equivalent, axial and circumferential strains, respectively
λ	ratio E_h/E
ρ	material density
ϕ	angle of rotation (Fig. 9)
φ	angle of rotation (Fig. 6)
σ_0, σ_e	material flow stress and equivalent stress, respectively
σ_x, σ_θ	axial and circumferential stress, respectively

The mixed collapse modes—global bending with progressively developed wrinkles, which are observed experimentally (Abramowicz and Jones, 1997; Karagiozova and Alves, 2004) and numerically (Karagiozova and Alves, 2004), suggest that 'rod' and 'shell' buckling modes co-exist in long tubes and they can develop simultaneously during impact. Moreover, two phases of deformation—initial compression and bending—characterise the response of shells that buckle in the plastic range. This particular feature means that the axially loaded elastic–plastic shells can be classified as 'Type II' structures, which are sensitive to the initial velocity (Su et al., 1995; Tam and Calladine, 1991; Zhang and Yu, 1989), striking mass (Tam and Calladine, 1991) and material properties (Karagiozova and Jones, 2001, 2002). A significant proportion of the initial kinetic energy can be absorbed during the first response phase of these structures, depending on how long the lateral inertia can support the unbuckled shape (Karagiozova et al., 2000; Karagiozova and Jones, 2002). Thus, the compressive phase can influence the initial conditions for the subsequent phase of deformation and in this way can affect the selection of the particular mode of collapse—global bending or progressive buckling (folding).

The influence of the material properties and loading parameters on the dynamic buckling mechanism is analysed in this paper using a two-phase concept, but no attempt has been made to study the influence of any mode interaction on the buckling transition. Elastic–plastic bilinear material models are used with the same characteristics as those of materials Mat1, Mat2 and Mat3 discussed in Part I (Karagiozova and Alves, 2004).

2. Mechanics of dynamic elastic–plastic buckling

2.1. Response of a circular shell to an axial impact

Inertia influences the response of a tube to an axial impact in a complex way affecting both the tendency of a long tube to buckle in a 'rod' mode (global bending) and the response of the tube to crush in a 'shell' mode (progressive buckling collapse). This can be seen when analysing the variation with time of some displacements and velocities associated with characteristic locations along the tube length.

Particular examples of the response of a tube with $L = 450$ mm made from material Mat2 and subjected to 5 kJ impacts are shown in Figs. 1 and 2. An initial velocity of 8.5 m/s causes global bending of the tube while the same tube responds by progressive buckling to a 8.75 m/s impact. Fig. 1(a) and (b) show the radial displacement–time histories at the tips of the wrinkles near to the proximal and distal end of the tube (labelled t and b in Fig. 3, respectively) together with lateral displacement at the location of the 'bending hinge', which is closest to the proximal end (labelled m in Fig. 3(b)). It is evident that, in both cases, i.e.

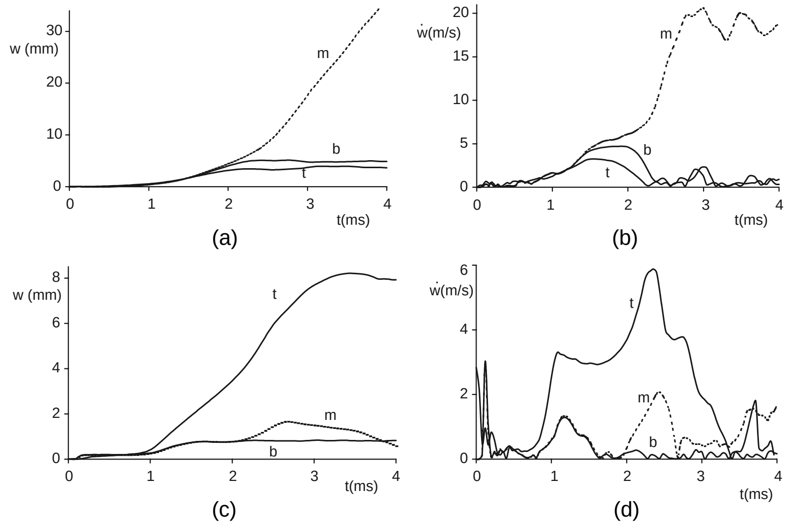

Fig. 1. (a)Displacement–time and (b) velocity–time behaviour of a tube with $L = 450$ mm subjected to a 5 kJ axial impact where $V_0 = 8.5$ m/s and undergoing global collapse. (c) and (d)—same as in (a) and (b) but for an impact velocity of 8.75 m/s, associated with progressive buckling (symbols t, m and b defined as in Fig. 3).

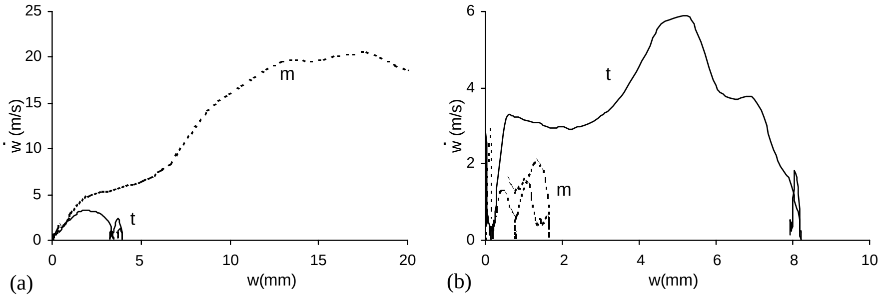

Fig. 2. Phase-plane diagrams associated with the tip of the top wrinkle (continuous line for *t* in Fig. 3) and 'bending hinge' (dashed line for *m* in Fig. 3) of a tube with length $L = 450$ mm undergoing (a) global collapse ($V_0 = 8.5$ m/s) and (b) progressive buckling ($V_0 = 8.75$ m/s).

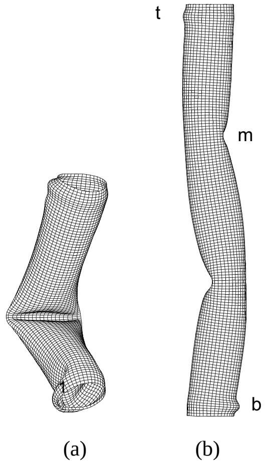

Fig. 3. Buckling modes. (a) a tube with $L = 300$ mm made from material Mat3; $V_0 = 2.5$ m/s, (b) a tube with $L = 450$ mm made from material Mat2; $V_0 = 6$ m/s.

global (lower velocity) and progressive (higher velocity) buckling, there is a distinguishing compressive phase, which lasts approximately 1.0 ms. The lateral displacements associated with all locations start to grow simultaneously, however, local buckling (a wrinkle) near to the proximal end of the tube develops more rapidly as indicated by the lateral displacement–time and the velocity–time histories in Fig. 1(c) and (d) (label *t*), which indicates progressive buckling for an impact with $V_0 = 8.75$ m/s. In contrast, global collapse occurs for $V_0 = 8.5$ m/s, when the growth of the lateral displacement at the location of the 'bending hinge' (label *m* in Fig. 1(a)) overtakes the increase of the local displacements.

The radial velocities associated with the maximum radial displacement of the first wrinkle and the lateral velocity at the location of the global 'bending hinge' presented in Fig. 1(b) and (d) for global bending and progressive buckling, respectively, show that in both cases, the maximum lateral velocity is associated with the corresponding buckling pattern. It is evident that larger velocities develop at the tip of the local wrinkle (label *t* in Fig. 1(d)) in the case of progressive buckling while the maximum lateral velocity for a global collapse is observed at the location of the global 'bending hinge' (label *m* in Fig. 1(b)).

Thus, the selection of the particular buckling pattern is a typical bifurcation problem as indicated by the phase-plane diagrams in Fig. 2. At the initiation of buckling, both modes of collapse have comparable velocities but a rapid increase of the velocity at the location of the particular unstable point (m in Fig. 2(a) or t in Fig. 2(b)) occurs, which leads to the development of large radial (progressive) or lateral (global) displacements. The displacements at points t and m in Fig. 2(a) and (b), respectively, do not grow with time as the corresponding velocities vanish as soon as the buckling pattern is selected.

An initial compression phase is a characteristic of the response of shells that buckle plastically and it can cause variation of the velocities at the outset of the second phase of deformation (global bending or progressive buckling). The influence of the material characteristics and loading parameters on these velocities is discussed in Sections 4.1 and 4.2.

3. Critical buckling length

It is interesting to observe that, except for some shells where $L = 300$ mm, the majority of the experimental and numerical results in Part I (Karagiozova and Alves, 2004) indicate that global buckling starts to develop in a mode that has the characteristics of the second axial buckling mode (a 'rod' mode). Some tubes develop later local wrinkles as well, which form the final mixed mode shape. Examples of the buckling patterns of a 300 and 450 mm long tubes are shown in Fig. 3. The buckling shape in Fig. 3(a) is close to the final shape of a short tube under a low velocity impact while the buckling shape in Fig. 3(b) represents a typical shape at the initiation of global bending of longer tubes when the impact velocity increases (Karagiozova and Alves, 2004).

These buckling patterns suggest that 'rod' models shown in Fig. 4 can be used to analyse the influence of the material parameters on the critical buckling lengths that mark the transition between progressive buckling and global collapse. The models consist of incompressible rods with a distributed mass $m = M/L$. It is assumed that the material is elastic–plastic with linear strain hardening, which is small, so that the rods in the models are subjected to a constant axial force, $A\sigma_0$. The cross-section area, A, of the rod and the corresponding inertia moment are equal to the cross-section area and the corresponding inertia moment, $\pi R^3 h$, of an actual shell, respectively. The experimental results and numerical simulations show that plastic bending deformations occur near to the shell ends as shown in Fig. 3. In the models, these deformations are taken into account as plastic bending moments in order to represent more realistically the boundary

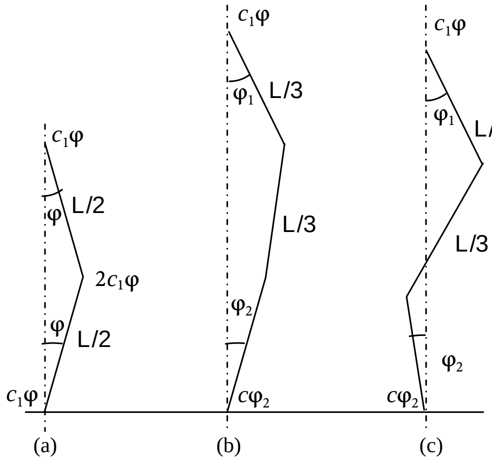

Fig. 4. 'Rod' modes for global bending of a circular shell; (a) Euler mode, (b) and (c) three-link models representing axial buckling modes.

conditions. It is assumed that the models in Fig. 4 are valid for small angles of rotation, therefore they can describe only the initiation of buckling but not the developed shapes of actual shells.

3.1. Euler buckling mode

The equation of motion of the model in Fig. 4(a) can be obtained from moment equilibrium as shown in Fig. 14 as

$$\frac{mL^3}{24}\ddot{\varphi} + \left(3c_1 - \frac{A\sigma_0 L}{2}\right)\varphi = 0, \tag{1}$$

where c_1 is a bending rigidity coefficient (see Section A.1)

$$c_1 = \frac{4E_h \pi R^3 h}{(1+\sqrt{\lambda})^2 L}, \tag{2}$$

E_h is the hardening modulus and $\lambda = E_h/E$. Thus, Eq. (1) can be presented as

$$\ddot{\varphi} - \frac{24}{\rho L^2}\left(\sigma_0 - \frac{12E_h R^2}{(1+\sqrt{\lambda})^2 L^2}\right)\varphi = 0. \tag{3}$$

It is evident that a positive coefficient before φ in Eq. (3) determines a solution with a hyperbolic function, therefore the critical length of a tube to buckle in an Euler mode is

$$L_{cr} = \frac{2R}{(1+\sqrt{\lambda})}\left(\frac{3E_h}{\sigma_0}\right)^{1/2}. \tag{4}$$

According to Eq. (4), the critical lengths of tubes with cross-section characteristics $2R = 50.8$ mm, $h = 2$ mm and made from materials Mat1, Mat2 and Mat3 are 114.8, 148.7 and 190.7 mm, respectively. Since the compressibility of the tubes is not taken into account, these values can be considered as a lower bound for the critical lengths of the corresponding tubes when subjected to static axial loads.

3.2. Second axial buckling mode

Long tubes can develop buckling modes higher then the Euler static buckling mode when subjected to an axial dynamic load (e.g. buckling modes that cause global collapse with two or more ‘bending hinges’ due to the ovalization of the tube cross-section). In particular, shapes with characteristics of the second buckling mode have been observed both experimentally and numerically. The three-link models in Fig. 4(b) and (c) can represent the second axial buckling mode of a shell and shapes between the Euler and second buckling mode depending on the angles φ_1 and φ_2.

Equilibrium of moments and forces acting on the two configurations (Fig. 15) is used to obtain the equations of motion for the configuration in Fig. 4(b),

$$\frac{2mL^3}{81}\ddot{\varphi}_1 + \frac{mL^3}{162}\ddot{\varphi}_2 + \left(6c - \frac{2L}{3}A\sigma_0\right)\varphi_1 - \left(4c - \frac{L}{3}A\sigma_0\right)\varphi_2 = 0, \tag{5}$$

$$\frac{mL^3}{162}\ddot{\varphi}_1 + \frac{2mL^3}{81}\ddot{\varphi}_2 - \left(4c - \frac{L}{3}A\sigma_0\right)\varphi_1 + \left(6c - \frac{2L}{3}A\sigma_0\right)\varphi_2 = 0 \tag{6}$$

and for the configuration in Fig. 4(c),

$$\frac{2mL^3}{81}\ddot{\varphi}_1 - \frac{mL^3}{162}\ddot{\varphi}_2 + \left(6c - \frac{2L}{3}A\sigma_0\right)\varphi_1 - \left(4c - \frac{L}{3}A\sigma_0\right)\varphi_2 = 0, \tag{7}$$

$$\frac{mL^3}{162}\ddot{\varphi}_1 - \frac{2mL^3}{81}\ddot{\varphi}_2 - \left(4c - \frac{L}{3}A\sigma_0\right)\varphi_1 - \left(6c - \frac{2L}{3}A\sigma_0\right)\varphi_2 = 0, \tag{8}$$

where c is a bending rigidity coefficient (see Eq. (A.16))

$$c = \frac{6E_{\mathrm{h}}\pi R^3 h}{(1+\sqrt{\lambda})^2 L}. \tag{9}$$

If the solution for φ_1 and φ_2 is sought in a form

$$\varphi_1 = D_1 \sin(\omega^2 t + \beta), \quad \varphi_2 = D_2 \sin(\omega^2 t + \beta), \tag{10}$$

the condition for a non-trivial solution of each system of differential equations that describes the motion of the models in Fig. 4(b) and (c) is obtained as a quadratic equation with respect to $(\omega)^2$,

$$\omega^4 - \frac{2.162}{15mL^3}[28c - 3A\sigma_0 L]\omega^2 + \frac{5.162}{15^2 m^2 L^6}[60c^2 - 16cA\sigma_0 L + (A\sigma_0 L)^2] = 0 \tag{11}$$

when substituting Eq. (10) into Eqs. (5)–(8). The solutions for φ_1 and φ_2 are characterised either by trigonometric or hyperbolic functions depending on the signs of the two roots of Eq. (11) (see Eq. (A.14)). An unstable response occurs when $(\omega_1)^2 > 0$ and $(\omega_2)^2 < 0$ or $(\omega_1)^2 > 0$ and $(\omega_2)^2 > 0$, so that the two roots of Eq. (11) determine two critical lengths for dynamic buckling associated with the three-link model as

$$L_{\mathrm{cr},1} = \frac{R}{(1+\sqrt{\lambda})}\left(\frac{18E_{\mathrm{h}}}{\sigma_0}\right)^{1/2} \tag{12}$$

and

$$L_{\mathrm{cr},2} = \frac{R}{(1+\sqrt{\lambda})}\left(\frac{30E_{\mathrm{h}}}{\sigma_0}\right)^{1/2}. \tag{13}$$

According to Eq. (12), the critical lengths for buckling of tubes with cross-section characteristics $2R = 50.8$ mm, $h = 2$ mm and made from materials Mat1, Mat2 and Mat3 are 140.5, 180.9 and 233.5 mm, respectively. According to Eq. (13), the critical lengths for the development of a second buckling mode in these tubes are 181.4, 233.5 and 301.5 mm, respectively. The above critical values (except for Mat3) are smaller than the shortest tubes of 300 mm, which are analysed numerically in Part I (Karagiozova and Alves, 2004). This explains why all examined 300 mm tubes can collapse in a global mode when subjected to a sufficiently low impact velocity (Fig. 5).

Eqs. (12) and (13) show that the critical buckling lengths of a circular shell with given cross-section characteristics are functions of the ratio E_{h}/σ_0. This dependence explains the different buckling modes that are observed in tubes with equal lengths but made from different materials when subjected to a low velocity impact. The Euler buckling mode occurs in a 300 mm long tube made from material Mat3 when subjected to a 2.5 m/s impact. In way of contrast, the 300 mm long tubes made from materials Mat1 and Mat2 develop ‘bending hinges’ at locations that are the characteristic of the second buckling mode. These tube start to buckle in the mode shown in Fig. 4(c) but the more rapid development of the ‘bending hinge’ that is closer to the proximal end of the shell causes the final buckling shapes presented in Fig. 5(a) and (b). The

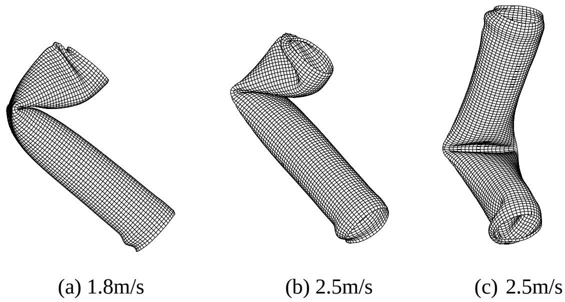

Fig. 5. Buckling shapes of 300 mm long tubes depending on the material properties. (a) Mat1, (b) Mat2, (c) Mat3.

length of 300 mm is between the two critical values for material Mat3, so that this shell buckles in an Euler mode. The length of 300 mm is larger than the second critical lengths for both Mat1 and Mat2, therefore these shells tend to develop the second buckling mode.

4. Tubes as Type II structures—two phase deformation concept

The critical lengths for global bending are obtained in Section 3 assuming that a shell deforms as an incompressible rod. In practice, however, shells much longer than $L_{\mathrm{cr},2}$ (Eq. (13)) may not develop global bending, which is evident from the numerical and experimental results presented in Part I (Karagiozova and Alves, 2004). The stabilisation of the response is caused by the increase of the impact velocity, which influences the shell compression (reduction of the overall length) and the speed of the development of a local wrinkle. Moreover, the interaction between the inertia of the striker and shell can influence the buckling pattern due to the variation of the absorbed energy during the initial compression phase.

The two phase deformation concept provides a tool for an analysis of 'Type II' structures. This approach was proposed by Tam and Calladine (1991) to explore the velocity and mass sensitivity of a simple plate structure and it is adopted here for the analysis of a tube response.

4.1. Phase 1—compression

The present analysis is focused on the second axial buckling mode that can develop in the case of global bending. The corresponding model shown in Fig. 6 consists of three rods, each of length $L/3$ with a distributed mass $m = M/L$. The rods are axially compressible by an amount $\Delta/3$, but do not deform due to the bending moments. This model is similar to the one shown in Fig. 4(c) but takes into account the compressibility of the shell.

The initial imperfections of the model have the expected buckling mode shape, $w_0 = \varphi_0 L/3$, so that equal, but opposite sign magnitudes at the end of the first and second link are assumed. The model in Fig. 6 is struck by a mass, G with an initial velocity, V_0 that causes an axial displacement, u, at the proximal end (see Section A.2.1).

$$u = L(\varphi_1^2 + \varphi_2^2 + \varphi_1\varphi_2 - 3\varphi_0^2)/3 + \Delta. \tag{14}$$

The deformed shape of the shell in Fig. 3(b) suggests that the angles of rotation φ_i can be assumed equal ($\varphi_1 = \varphi_2 = \varphi$) during the compression phase, so that the vertical displacement of the proximal end of the model is

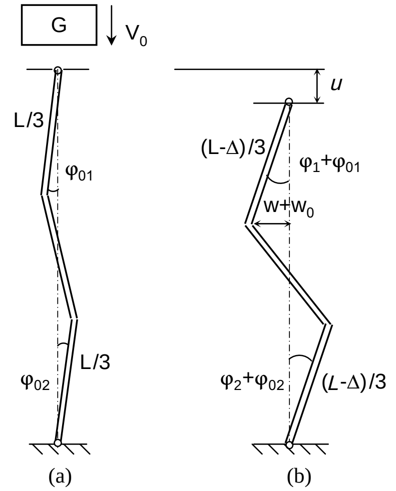

Fig. 6. Model for the initial compressive phase (global bending).

$$u = L(\varphi^2 - \varphi_0^2) + \Delta \tag{15}$$

and the corresponding axial velocity is

$$\dot{u} = 2L\varphi\dot{\varphi} + \dot{\Delta}. \tag{16}$$

For small angles of rotation $\varphi = w/(L/3)$, therefore

$$V_{\text{model}} = \dot{u} = \frac{18}{L} w\dot{w} + \dot{\Delta} = V_1 + \dot{\Delta}, \tag{17}$$

when adopting

$$V_1 = \frac{18}{L} w\dot{w}. \tag{18}$$

If the angles of rotation are equal, Eqs. (7) and (8) reduce to a single equation of motion

$$\frac{mL^3}{54}\ddot{\varphi} + (10c - A\sigma_0 L)\varphi = 0 \tag{19}$$

and for small angles φ

$$\ddot{w} = \frac{54\sigma_0}{\rho L^2}\left(1 - \frac{30E_{\text{h}}R^2}{\sigma_0(1+\sqrt{\lambda})^2 L^2}\right)w. \tag{20}$$

The solution of Eq. (20) is

$$w = w_0 \cosh(\gamma t) \tag{21}$$

when applying the initial conditions $w(0) = w_0$ and $\dot{w}(0) = 0$ and where

$$\gamma = \frac{3}{L}\sqrt{\frac{6\sigma_0}{\rho}}\sqrt{1 - \frac{30E_{\text{h}}R^2}{\sigma_0(1+\sqrt{\lambda})^2 L^2}} \tag{22}$$

and ρ is the material density. Thus, the axial velocity of the model due to the rotations of the links is

$$V_1 = \frac{9\gamma w_0^2}{L}\sinh(2\gamma t). \tag{23}$$

The equation of motion of the striker is

$$G\dot{V} = -A\sigma_0, \tag{24}$$

so that the corresponding velocity is

$$V = V_0 - \frac{A\sigma_0}{G}t. \tag{25}$$

A plot of the velocities V_1 and V given by Eqs. (23) and (25) is presented in Fig. 7 for a shell with $2R = 50.8$ mm, $h = 2$ mm and $L = 450$ mm. The intersection of the two curves defines the configuration at the end of the initial compression phase at $t = t^*$ since Eq. (17) gives $\dot{\Delta} = 0$. The area between the ordinate axis and the two curves $(V - V_1)$ in Fig. 7 gives the total shortening of the model, which is proportional to the absorbed energy during the first phase (Tam and Calladine, 1991).

According to Eqs. (23) and (25), the proportion of the initial impact energy absorbed during the initial compression phase depends on both the material characteristics and loading parameters. For the same impact mass, G, and velocity V_0, a material having a lower yield stress will absorb a smaller proportion of the initial energy thus leaving more energy for the bending phase. Therefore, a larger proportion of the initial kinetic energy remains for the bending phase of a shell made from material Mat3 due to the lower flow stress compared to material Mat2. Moreover, the initial momentum (GV^*) at the outset of the bending phase is higher in a tube made from material Mat3, which results in a higher initial angular velocity $\dot{\varphi}(t^*)$ at the outset of the bending phase.

It is evident in Fig. 3 that 'plastic hinges' develop due to the ovalisation of the shell cross-section, so that energy proportional to the plastic moments $M_p(\varphi, \sigma_0)$ dissipates during the phase of global collapse (Wierzbicki and Sinmao, 1997). Thus, bending deformations develop more rapidly in a shell made from material Mat3 due to the smaller bending resistance to a global collapse.

This scenario predicts that if a tube made from material Mat2 buckles progressively at the transition impact velocity, the same geometry tube made from material Mat3 will buckle globally when subjected to

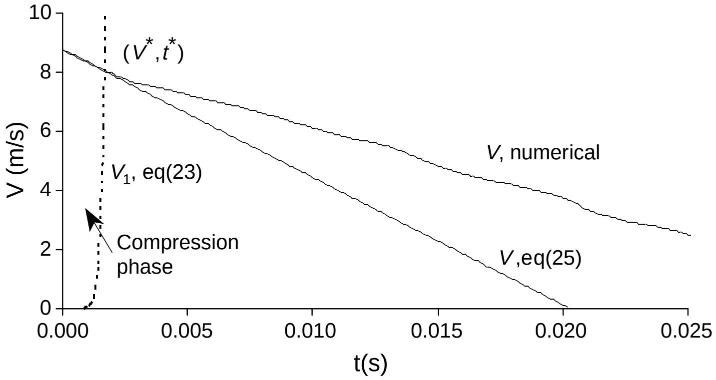

Fig. 7. Theoretical predictions for velocities V_1 and V according to Eqs. (23) and (25) for a model of a tube with $L = 450$ mm and $\sigma_0 = 175$ MPa under an impact with $V_0 = 8.75$ m/s, $G = 120$ kg in comparison with the numerical prediction for the axial velocity of the proximal end, $V_{\text{numerical}}$, of the same tube; $w_0 = 0.0005L$.

an impact with the same loading parameters. In order to stabilise the response of a tube made from material Mat3, the impact velocity should be increased, which causes additional energy to be absorbed during the initial compression phase. The increase of the initial velocity leads to a decrease of the striking mass, which will additionally increase the proportion of the absorbed energy during the compression phase according to Eq. (25). In this way, the initial momentum (GV^*) decreases, which results in a lower initial angular velocity for the bending phase.

The variation of the striker velocity, V, that is associated with the transition velocity for shells made from Mat2 ($\sigma_0 = 175$ MPa) and Mat3 ($\sigma_0 = 105$ MPa) and the variation of the axial velocity of the model in Fig. 6 with time, V_1, are illustrated in Fig. 8 for particular shells having lengths of 450 mm (Fig. 8(a)) and 630 mm (Fig. 8(b)). It is evident that at the transition velocities, the compression phase in shells with equal lengths lasts longer in a shell made from the material with a lower yield stress provided that both materials have identical strain hardening characteristics. During this time, the absorbed energy continues to increase, thereby approaching the energy absorbed during the compression phase of a shell with a higher yield stress (Table 1), which commences to bend more rapidly. One can see that the bending energy, $T_b = G(V^*)^2/2$, decreases when increasing the impact velocity and length of the shells for both materials.

The present analysis shows that smaller momentum (GV^*) should be achieved in a shell made from material Mat3 in comparison to a shell made from Mat2 (Table 1) in order to stabilize the response. These smaller values are necessary for a stabilization due to the smaller resistance to a global collapse of a shell made from Mat3. This explains the departure (from each other) of the curves that mark the critical buckling lengths for materials Mat2 and Mat3 in Fig. 6, Part I (Karagiozova and Alves, 2004) for impact velocities higher than 8 m/s.

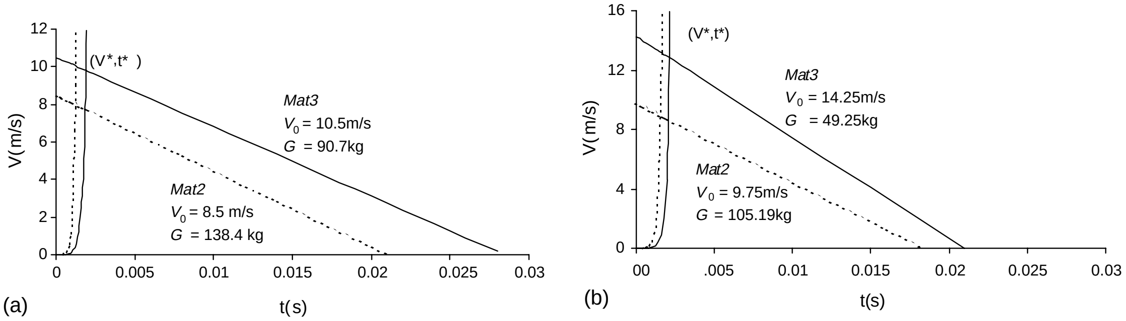

Fig. 8. Variation of the velocity of the striker and axial velocity of the model in Fig. 6 with time for a shell with $h = 2$ mm, $R = 25$ mm; Mat2—dashed line, Mat3—solid line, (a) $L = 450$ mm, (b) $L = 630$ mm.

Table 1
Comparison between the kinetic energies available for the bending phase, T_b, at some transition impact velocities depending on the material yield stress and loading parameters when using Eqs. (23) and (25) to obtain V^* and t^*; $T_0 = 5$ kJ

L (mm)	V_0 (m/s)	G (kg)	Material	V^* (m/s)	t^* (ms)	T_b (J)	GV^* (kg m/s)
450	8.50	138.4	Mat2	8.04	1.183	4473.2	1112.8
450	10.5	90.70	Mat3	9.87	1.687	4415.2	894.9
540	9.25	116.87	Mat2	8.63	1.348	4352.1	1008.6
540	12.75	61.52	Mat3	11.77	1.830	4260.7	724.1
630	9.75	105.19	Mat2	8.96	1.528	4222.4	942.5
630	14.25	49.25	Mat3	12.87	2.053	4082.4	633.8

The analysis of the response of the model in Fig. 6 in terms of energy absorption shows that the initial compression phase in a circular tube plays a significant role for the buckling transition causing variation of the initial conditions for the bending phase. This model reveals the importance of the material yield stress and inertia properties of the striker for the energy partitioning in dynamically loaded circular shells.

4.2. Phase 2—buckling

4.2.1. A simple model for the development of a single wrinkle

The rapid development of local wrinkling is another factor that stabilises the response of a tube subjected to an axial impact thus increasing the critical length for buckling transition beyond $L_{\mathrm{cr},2}$ (Eq. (13)). The numerical simulations show that the material strain hardening properties influence the critical shell length for transition between the two buckling modes (Fig. 6 in Part I (Karagiozova and Alves, 2004)). The smaller bending rigidity of material Mat1 in comparison to material Mat2 allows wrinkles to develop more rapidly soon after the impact, which stabilises the response, leading the shell to absorb the initial kinetic energy also by folding.

A simplified model for the initiation of progressive buckling (a 'folding model') can be developed assuming that a single wrinkle occurs initially while the rest of the shell stays undeformed (Alexander, 1969). The shell thickness is small in comparison to the other shell dimensions, so that the plane stress approximation gives an adequate description of the stress state in a circular shell. The proposed model aims to explore the influence of material hardening and the loading conditions on the bending deformation associated with progressive buckling.

It is observed experimentally (Fig. 4 (upper row) in Part I (Karagiozova and Alves, 2004)) that the first wrinkle in a circular shell usually develops axisymmetrically, so that this assumption is used for the model in Fig. 9 to represent a single wrinkle. The links of the model represent a part of a shell strip with length $2l$ ($l = 1.34\sqrt{Rh}$ (Jones, 1989)) and thickness h. The mass of the model, m^*, is equal to the mass per unit circumferential length of a single axisymmetric wrinkle in an actual shell and $m^* = 2l\rho h$. It is assumed that the links are incompressible and rotate only as rigid bodies. The material properties of a shell are modelled by the characteristics of the springs in each cell that represent the axial, F_i^s, and radial forces, F_i^c, where $i = 1, 2, 3$. The strain distribution across the shell thickness is modelled by a number of springs $k = 1, \dots, 2n_t + 1$ in each cell, where the number of the discrete intervals is $2n_t$.

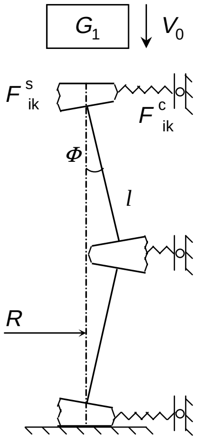

Fig. 9. Model for the buckling phase (first local wrinkle for progressive buckling).

The equation of motion of the model in Fig. 9 is (see Section B.1)

$$\ddot{\phi} = -\frac{2l^2(m^* + G_1)\dot{\phi}^2 \sin\phi\cos\phi + M_1(t) + M_2(t) + 0.5F^c(t)l^2\cos\phi}{2l^2[m^*/3 + (m^* + G_1)\sin^2\phi]}, \tag{26}$$

where $G_1 = G/2\pi R$, $M_1(t)$ and $M_2(t)$ are the bending moments. Bending moments M_1 are associated with the top and bottom cells ($i = 1, 3$) while M_2 is defined for the middle cell ($i = 2$). F^c is a distributed force along l, which accounts for the circumferential forces F^θ_{ik} and is defined by the forces $F^c_{ik} = F^\theta_{ik}/R$ (see Section B.1).

It is assumed that the model in Fig. 9 is subjected to an impulsive load $I = G_1V_0$, so that the initial conditions can be obtained using Lagrange's equation, which gives

$$\dot{\phi}_{|t=0} = \frac{G_1V_0\sin\phi_0}{[m^*/3 + (m^* + G_1)\sin^2\phi_0]l}, \tag{27}$$

where ϕ_0 is the initial imperfection taken as $\phi_0 = w_0/l$.

The material of the model in Fig. 9 is elastic–plastic with linear strain hardening, E_h, in the true stress–true strain domain. The Tresca yield criterion is used to obtain explicit expressions for the stress increments $\mathrm{d}\sigma_x$ and $\mathrm{d}\sigma_\theta$ as functions of the strain increments in a circular shell, $\mathrm{d}\varepsilon_x$ and $\mathrm{d}\varepsilon_\theta$ (Karagiozova and Jones, 2000). The strains in the top and bottom cells are defined as

$$\varepsilon_x(z)_1 = \varepsilon_x(z)_3 = -z\sin\phi/l, \quad \varepsilon_\theta = 0, \tag{28a,b}$$

while for the middle cell

$$\varepsilon_x(z)_2 = 2z\sin\phi/l, \quad \varepsilon_\theta = w/R, \quad w = l\sin\phi \tag{29a,b}$$

for $-h/2 \leqslant z \leqslant h/2$ and $\phi_0 \leqslant \phi < \pi/2$. Therefore, the axial strains in the discrete points across the cells of the model in Fig. 9 are

$$\varepsilon_x(z_k)_1 = \varepsilon_x(z_k)_3 = -\frac{(k - n_t - 1)h}{2n_tl}\sin\phi, \quad k = 1, \ldots, 2n_t + 1 \tag{30}$$

and

$$\varepsilon_x(z_k)_2 = \frac{(k - n_t - 1)h}{n_tl}\sin\phi, \quad k = 1, \ldots, 2n_t + 1. \tag{31}$$

The expressions $\mathrm{d}\sigma_x = f_1(\mathrm{d}\varepsilon_x, \mathrm{d}\varepsilon_\theta, \sigma_0, E, E_\mathrm{h})$ and $\mathrm{d}\sigma_\theta = f_2(\mathrm{d}\varepsilon_x, \mathrm{d}\varepsilon_\theta, \sigma_0, E, E_\mathrm{h})$ for each side of the Tresca hexagon (see Section B.2) are used to calculate the generalised forces M_1, M_2 and F^c as

$$\mathrm{d}M_i = \cos\phi\frac{h}{2n_t}\sum_{k=1}^{2n_t+1}(k - n_t - 1)\,\mathrm{d}F^s_{ik}, \quad \mathrm{d}F^s_{ik} = \frac{h}{(2n_t + 1)}\mathrm{d}\sigma^x_{ik}, \qquad i = 1, 2, \tag{32}$$

$$\mathrm{d}F^c_i = \sum_{k=1}^{2n_t+1}\mathrm{d}F^c_{ik} = \frac{1}{R}\sum_{k=1}^{2n_t+1}\mathrm{d}F^\theta_{ik}, \quad \mathrm{d}F^\theta_{ik} = \frac{h}{(2n_t + 1)}\mathrm{d}\sigma^\theta_{ik}, \qquad i = 1, 2. \tag{33}$$

It is assumed that the buckling commences after compression in the plastic range, so that the following initial conditions are adopted for the analysis of the response of the buckling model

$$\sigma^x_{ik}(t = 0) = -\sigma_0, \quad \sigma^\theta_{ik}(t = 0) = 0, \qquad i = 1, 2, 3, \quad k = 1, \ldots, 2n_t + 1. \tag{34}$$

Eq. (26) with the initial condition (27) is solved numerically using the NAG Fortran Library when the variation of the bending moments M_i and the radial force F^c with time are calculated at the discrete intervals (Δt) using Eqs. (32) and (33).

4.2.2. Influence of the material strain hardening and loading parameters

It is evident from Eqs. (26)–(34) that the material characteristics (the yield stress and strain hardening) and the initial conditions for the bucking phase influence the response of the model in Fig. 9. Comparison between the development of the lateral displacement w for materials Mat1 ($\lambda = 0.0043$) and Mat2 ($\lambda = 0.007$) is shown in Fig. 10 where it is evident that the lower hardening characteristics contribute to a more rapid buckling.

It should be noted that the model for the buckling phase does not take into account the initial compression and the reduction of the axial velocity, so that V_0 is used in the calculations instead of V^* obtained in Section 4.1. In fact, the actual initial velocity for the buckling phase of a shell made from material Mat1 is higher in comparison to the velocity in a Mat2 shell. The higher initial velocity at the outset of the buckling phase also contributes to the more rapid development of the lateral displacements and the formation of a wrinkle, which stabilises the tube response. This behaviour indicates that a local wrinkle can develop more rapidly in a shell made from material Mat1 leading eventually to a stabilisation of the response for lower impact velocities in comparison to a shell made from Mat2 as it is indicated in Fig. 6, Part I (Karagiozova and Alves, 2004).

In this scenario, the bending rigidity can influence the location of the first wrinkle in identical shells subjected to similar loading conditions but made from different materials. A 5 kJ axial impact on a 360 mm long shell causes the first wrinkle to develop near to the proximal end of a shell made from material Mat1, while the first wrinkle in a shell made from material Mat2 develops near to the distal end (Fig. 11).

The influence of the initial conditions on the growth of the lateral displacements, w, of the model in Fig. 9 is illustrated in Fig. 12(a) for impacts with constant initial kinetic energy, but applied with different impact velocities and assuming the characteristics of a shell made from material Mat1. One can see that a larger mass applied with a lower initial velocity causes more rapid development of the bending deformations. This response could be attributed to inertia effects in a shell only but, in fact, the inertia of the striking mass influences the response as well. The model buckles more rapidly when struck by a larger mass ($G = 219.48$ kg vs. $G = 130$ kg), even if both impacts are applied with an equal initial velocity of 8.75 m/s (Fig. 12(b)).

The initial condition (Eq. (27)) for the response of the model in Fig. 9 suggests that the initial angular velocity $\dot{\phi}$ is constant for a constant initial momentum GV_0. It is evident in Fig. 12(c) that, even if subjected to impacts with equal initial momentum, the model in Fig. 9 buckles more rapidly under the impact with $G = 219.48$ kg, $V_0 = 8.75$ m/s. This response is caused by the larger bending deformations that develop soon after an impact with a larger mass.

The influence of the initial velocity for a constant striking mass on the bending phase is illustrated in Fig. 12(d). An impact with $G = 219.48$ kg and $V_0 = 8.75$ m/s causes more rapid development of the lateral displacements w in comparison to the 6.75 m/s impact. However, the maximum displacement $w = l$ is achieved at the same time in both cases.

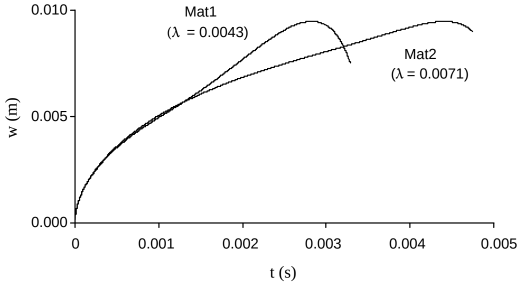

Fig. 10. Development of the lateral displacement, w, of the model in Fig. 9 depending on the material hardening, $h = 2$ mm, $R = 25$ mm; $V_0 = 8.75$ m/s, $G = 130.61$ kg.

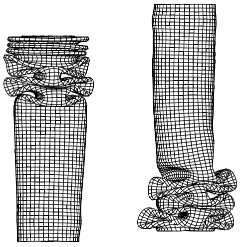

(a) 4.15m/s (b) 4.0m/s

Fig. 11. Location of the wrinkles depending on the material hardening. (a) Mat1: $E_h = 300$ MPa, (b) Mat2: $E_h = 500$ MPa.

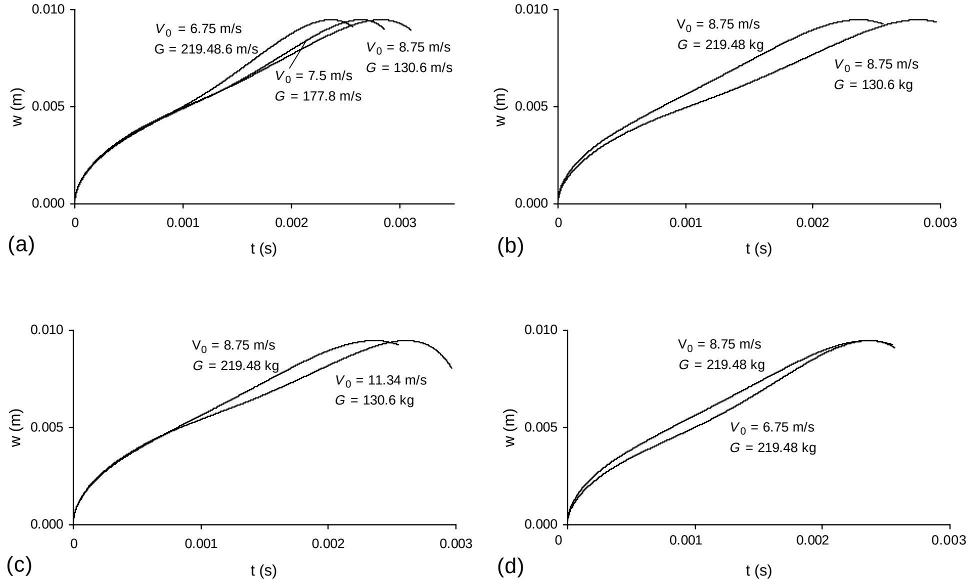

Fig. 12. Development of the lateral displacement, w, in the model in Fig. 9 with $h = 2$ mm, $R = 25$ mm and material Mat1. (a) Equal initial kinetic energy, $T_0 = 5$ kJ, (b) Equal initial velocity $V_0 = 8.75$ m/s, (c) Equal initial momentum $GV_0 = 1481.14$ kg.m/s, (d) Constant striking mass $G = 219.48$ kg.

The speed of the development of a local wrinkle can be a factor causing an *anomalous* response for some impact velocities, e.g. in Fig. 11 in Part I (Karagiozova and Alves, 2004). An impact with $V_0 = 6.75$ m/s and $G = 219.48$ kg causes the first wrinkle to develop near to the proximal end (Fig. 11(b) in Part I (Karagiozova and Alves, 2004)). However, an impact with a smaller mass ($G = 177.8$ kg) and $V_0 = 7.5$ results in a lower speed of the development of a wrinkle near to the proximal end due to the increased inertia. Meanwhile, the global lateral displacements continue to grow, so that the shell buckles in a global mode (Fig. 11(c) in Part I (Karagiozova and Alves, 2004)).

4.3. Influence of the strain rate effects on the local buckling phase

The numerical simulations presented in Part I (Karagiozova and Alves, 2004) reveal that the strain rate effects cause a destabilisation of a circular shell subjected to an axial impact. A reason for such kind of response can be related to the variation of the hardening characteristics during the buckling phase, which controls the development of a local wrinkle. In this Section, the effect of the material strain rate sensitivity on the buckling phase is estimated for the case of progressive buckling of a shell with $L = 450$ mm made from material Mat2 and subjected to an impact with $V_0 = 8.75$ m/s and $G = 219.48$ kg.

The displacement–time, $w(t)$ and velocity–time histories, $\dot{w}(t)$, associated with the tip of the local wrinkle near to the proximal end of a shell (Fig. 1(c) and (d)) are used to estimate the effects of the strain rate on buckling when the Cowper–Symonds equation is employed with $D = 1\,288\,000$ s^{-1} and $q = 4$ (Alves, 2000; Jones, 1974). The same parameters are used in Part I (Karagiozova and Alves, 2004) to simulate the strain rate effects on the dynamic buckling transition. It is evident from these figures that the compressive phase continues until $t^* \approx 0.9$ ms when a rapid growth of the radial displacement, w, commences. After this time, the bending deformations dominate, so that it can be assumed that, after the compressive phase, the stress-state is characterised by $\sigma_x = 0$, $\sigma_\theta > 0$. Then, it can be shown that $\sigma_e = \sigma_\theta$ and $\dot{\varepsilon}_e = \dot{\varepsilon}_\theta$ when using the relationships

$$\sigma_x = \frac{2\sigma_e}{3\dot{\varepsilon}_e}(2\dot{\varepsilon}_x + \dot{\varepsilon}_\theta), \quad \sigma_\theta = \frac{2\sigma_e}{3\dot{\varepsilon}_e}(\dot{\varepsilon}_x + 2\dot{\varepsilon}_\theta), \tag{35}$$

and

$$\dot{\varepsilon}_e = \frac{2}{\sqrt{3}}(\dot{\varepsilon}_x^2 + \dot{\varepsilon}_\theta^2 + \dot{\varepsilon}_x\dot{\varepsilon}_\theta)^{1/2} \tag{36}$$

for a plane stress problem and the von Mises yield criterion.

The circumferential strain is $\varepsilon_\theta = w/R$, therefore $\dot{\varepsilon}_\theta = \dot{w}/R$. Further, the dynamic equivalent stress can be obtained from the Cowper–Symonds equation as

$$\sigma_e^{\text{dynamic}}(\varepsilon_e) = \sigma_e^{\text{static}}(\varepsilon_e)\left[1 + \left(\frac{\dot{w}}{RD}\right)^{1/q}\right], \tag{37}$$

where

$$\sigma_e^{\text{static}}(\varepsilon_e) = \sigma_\theta(\varepsilon_\theta) = \sigma_0 + E_h\varepsilon_\theta. \tag{38}$$

The stress–strain histories during the bending phase for the loading parameters in Fig. 1(c,d) are shown in Fig. 13 for a strain rate insensitive material (Mat2) and a strain rate sensitive material according to

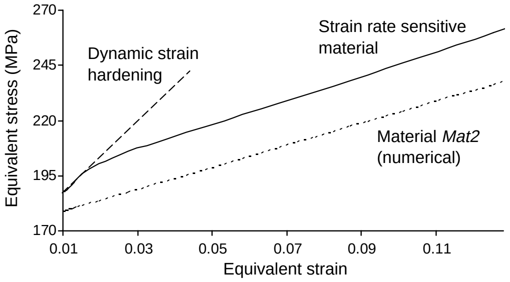

Fig. 13. Variation of the stress with strain at the tip of a local wrinkle during buckling of a shell with $2R = 50.8$ mm, $h = 2$ mm and $L = 450$ mm made of material Mat2 (numerical simulation) and when taking into account the strain rate effects according to Eq. (37); $V_0 = 8.75$ m/s, $G = 219.48$ kg.

Eq. (37). It is evident that the initial bending starts to develop with considerably higher strain hardening when the strain rate effects are taken into account. The initial strain hardening modulus is estimated as $E_\mathrm{h} = 2030$ MPa ($\lambda = 0.029$), which is four times larger than the strain hardening modulus $E_\mathrm{h} = 500$ MPa for Mat2. It was already shown in Section 4.2.2 that the increase of the strain hardening delays the development of a local wrinkle. Therefore, if a shell made from a strain rate insensitive material buckles progressively at a transition impact velocity, it is likely to respond by a global bending when the material exhibits strain rate effects, as shown in Figs. 13 and 14 in Part I (Karagiozova and Alves, 2004).

5. Conclusions

The mechanics of the transition from dynamic progressive buckling to global bending collapse of axially loaded circular tubes described in Section 2 characterises all the tubes analysed in the present study and discussed in Part I (Karagiozova and Alves, 2004) regardless of the tube lengths, impact velocity and material properties. This type of response allowed to employ the two-phase concept for deformation of circular tubes in order to provide some insight into the dynamic buckling transition phenomenon. The influence of the material properties and loading parameters on the selection of the collapse mode of tubes with a particular ratio $2R/h$ is analysed using two simple models. The first model is associated with the compression phase in the case of a global collapse and the second one models the development of a single wrinkle when a circular shell starts to buckle progressively.

The initial compression phase is governed primarily by the material yield stress, inertia properties of the shell and the interaction between the striker and shell as shown in Section 4.1. This phase causes variation of the initial conditions for the subsequent phase of bending or folding depending on the energy absorbed by compression. Thus, materials having higher yield stress are desirable in order to increase the proportion of the external impact energy absorbed in the initial compression phase and, perhaps, to increase the bending rigidity during the subsequent ovalisation of the tube cross-section in the case of global bending (Wierzbicki and Sinmao, 1997).

The folding phase is clearly dependent on the material strain hardening that controls the speed of the development of the first local wrinkle, as shown in Section 4.2.2. A delay of the development of a local wrinkle in a tube would favour a ‘rod’ buckling mode and consequently a global collapse. Thus, materials with low strain hardening characteristics could have a better performance by causing a rapid development of the first wrinkle and therefore stabilisation of the response. It is shown in Section 4.3 that larger material strain hardening during the early stage of the shell response, which is characteristic of strain rate sensitive materials causes a destabilisation of the shell by decreasing the speed of the development of the first wrinkle, which then favours global bending.

The theoretical analysis of the influence of various factors on particular phases of the dynamic buckling of long tubes presents an explanation for some of the observed phenomena in Part I (Karagiozova and Alves, 2004). However, the mode interaction, which is an essential feature of the buckling transition remains to be explored and this will be the subject of a further study.

Acknowledgements

The support from the Brazilian funding agency, FAPESP through grants 99/09871-5 and 00/08446-8 and from the Bulgarian National Research Fund, contract TH-1103/01 is greatly acknowledged.

Appendix A. Global bending

A.1. Euler buckling mode

The forces and moments that act on a two-link model are shown in Fig. 14. The bending moments at A, B and C are characterised by a bending rigidity c_1, which is calculated when using the reduced modulus, $E_r = 4EE_h/(\sqrt{E} + \sqrt{E_h})^2$, for a material with linear strain hardening. The bending moment at location B in Fig. 14 is

$$M_B = E_r I \kappa, \tag{A.1}$$

where the inertia moment $I = \pi R^3 h$ and the curvature at this point is taken as $\kappa = 2\varphi/L$ (Wierzbicki and Sinmao, 1997), so that

$$c_1 = \frac{4E_h \pi R^3 h}{(1 + \sqrt{\lambda})^2 L}. \tag{A.2}$$

A.2. Second axial buckling mode

A three-link model under axial compression can develop either of the shapes shown in Fig. 4. The equations of motion of links AB and CD in Fig. 15 are obtained from moment equilibrium with respect to points A and D, respectively

$$\frac{mL^3}{81}\ddot{\varphi}_1 + c(3\varphi_1 - \varphi_2) - \frac{PL}{3}\varphi_1 + X_1\frac{L}{3} = 0 \tag{A.3}$$

and

$$\frac{mL^3}{81}\ddot{\varphi}_2 + c(3\varphi_2 - \varphi_1) - \frac{PL}{3}\varphi_2 + X_2\frac{L}{3} = 0. \tag{A.4}$$

The equation of motion of link BC is obtained from moment equilibrium with respect to the center of the mass

$$\frac{mL^3}{324}(\ddot{\varphi}_1 - \ddot{\varphi}_2) + c(2\varphi_1 - \varphi_2) - c(2\varphi_2 - \varphi_1) - \frac{PL}{3}(\varphi_1 - \varphi_2) + X_1\frac{L}{6} - X_2\frac{L}{6} = 0 \tag{A.5}$$

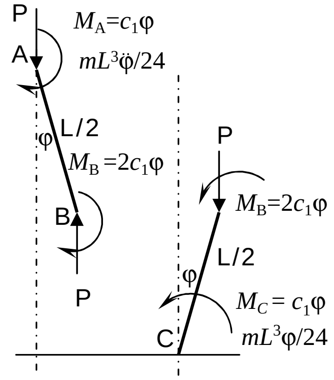

Fig. 14. Forces and moments in a 'rod' model representing an Euler buckling mode.

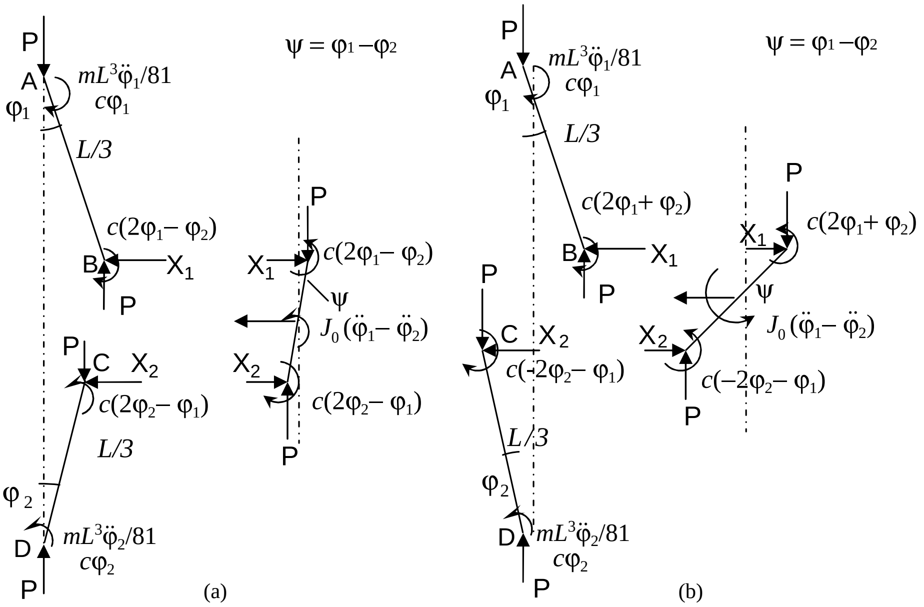

Fig. 15. Forces and moments in a three-link model. (a) First buckling mode; (b) Second buckling mode.

and the sum of the projection of all forces on the horizontal axis is

$$\frac{mL^2}{18}(\ddot{\varphi}_1+\ddot{\varphi}_2)-X_1-X_2=0. \tag{A.6}$$

The equations of motion for the shape in Fig. 15(a) are obtained as

$$\frac{2mL^3}{81}\ddot{\varphi}_1+\frac{mL^3}{162}\ddot{\varphi}_2+\left(6c-\frac{2L}{3}P\right)\varphi_1+\left(4c-\frac{L}{3}P\right)\varphi_2=0 \tag{A.7}$$

and

$$\frac{mL^3}{162}\ddot{\varphi}_1+\frac{2mL^3}{81}\ddot{\varphi}_2-\left(4c-\frac{L}{3}P\right)\varphi_1+\left(6c+\frac{2L}{3}P\right)\varphi_2=0, \tag{A.8}$$

when determining the forces X_1 and X_2 from Eqs. (A.5) and (A.6) and substituting the corresponding expressions into Eqs. (A.3) and (A.4).

The equations of motion of the model in Fig. 15(b) are obtained using the equilibrium of moments and forces as

$$\frac{2mL^3}{81}\ddot{\varphi}_1-\frac{mL^3}{162}\ddot{\varphi}_2+\left(6c-\frac{2L}{3}P\right)\varphi_1-\left(4c-\frac{L}{3}P\right)\varphi_2=0 \tag{A.9}$$

and

$$\frac{mL^3}{162}\ddot{\varphi}_1-\frac{2mL^3}{81}\ddot{\varphi}_2-\left(4c-\frac{L}{3}P\right)\varphi_1-\left(6c+\frac{2L}{3}P\right)\varphi_2=0. \tag{A.10}$$

The solution for φ_1 and φ_2 for the systems of Eqs. (A.7)–(A.10) can be sought in a form

$$\varphi_1=D_1\sin(\omega^2t+\beta),\quad \varphi_2=D_2\sin(\omega^2t+\beta). \tag{A.11}$$

After substituting these expressions into the corresponding equations, the condition for a non-trivial solution of either of the systems (A.7) and (A.8) or (A.9) and (A.10) is obtained as,

$$\begin{vmatrix} \left(6c-\frac{2PL}{3}\right)-\frac{2ml^3}{81}\omega^2 & \left(4c-\frac{PL}{3}\right)-\frac{ml^3}{162}\omega^2 \\ -\left[\left(4c-\frac{PL}{3}\right)-\frac{ml^3}{162}\omega^2\right] & -\left[\left(6c-\frac{2PL}{3}\right)-\frac{2ml^3}{81}\omega^2\right] \end{vmatrix}=0, \tag{A.12}$$

which gives

$$\omega^4-\frac{2.162}{15mL^3}[28c-3PL]\omega^2+\frac{5.162}{15^2m^2L^6}[60c^2-16cPL+(PL)^2]=0 \tag{A.13}$$

with roots

$$(\omega_1)^2=\frac{54}{15mL^3}(6c-PL),\quad (\omega_2)^2=\frac{5.54}{15mL^3}(10c-PL). \tag{A.14}$$

In Eqs. (A.3)–(A.14), $P=A\sigma_0$ and c is a bending rigidity coefficient, which is obtained when using the reduced modulus, E_r, for a linear strain hardening material. In Fig. 15(a,b),

$$M_\mathrm{B}=E_\mathrm{r}I\kappa \tag{A.15}$$

where the curvature κ is taken as $\kappa=\alpha/(2L/3)$, where α is the angle between two joint links, so that

$$c=\frac{6E_\mathrm{h}\pi R^3h}{(1+\sqrt{\lambda})^2L}. \tag{A.16}$$

A.2.1. Vertical displacements for the three-link model

The vertical displacement of the proximal ends of the models in Fig. 4(b) and (c) can be expressed as

$$u=\{[L\cos\varphi_{01}-(L-\Delta)\cos\varphi_1]+[L\cos\varphi_{02}-(L-\Delta)\cos\varphi_2]+[L\cos\psi_0-(L-\Delta)\cos\psi]\}/3, \tag{A.17}$$

assuming that these models have certain initial imperfections. The angles φ_{01} and φ_{02} are the initial angles of links AB and CD, respectively and the initial angle of the middle link, ψ_0, is a function of φ_{01} and φ_{02}. For small angles $\cos\varphi_i\approx 1-\varphi_i^2/2$, therefore

$$u=L[(\varphi_1^2/2+\varphi_2^2/2+\psi^2/2)-(\varphi_{01}^2/2+\varphi_{02}^2/2+\psi_0^2/2)]/3+\Delta(3-\varphi_1^2/2-\varphi_2^2/2-\psi^2/2)/3. \tag{A.18}$$

or

$$u=L[(\varphi_1^2/2+\varphi_2^2/2+\psi^2/2)-(\varphi_{01}^2/2+\varphi_{02}^2/2+\psi_0^2/2)]/3+\Delta \tag{A.19}$$

when taking into account that $\varphi_i\ll 1$.

Initial imperfections for the model configuration in Fig. 4(b) given by $\varphi_0=\varphi_{01}=\varphi_{02}$ lead to

$$(\varphi_{01}^2/2+\varphi_{02}^2/2+\psi_0^2/2)=(\varphi_{01}^2+\varphi_{02}^2-\varphi_{01}\varphi_{02})=\varphi_0^2, \tag{A.20}$$

where $\psi_0=\varphi_{01}-\varphi_{02}$. The assumption that $\varphi_0=\varphi_{01}=-\varphi_{02}$ for the model configuration in Fig. 4(c) leads to

$$(\varphi_{01}^2/2+\varphi_{02}^2/2+\psi_0^2/2)=(\varphi_{01}^2+\varphi_{02}^2/+\varphi_{01}\varphi_{02})=3\varphi_0^2, \tag{A.21}$$

where $\psi_0 = \varphi_{01} + \varphi_{02}$. The vertical displacements that occur in the two configurations of the three-link model are

$$u = L(\varphi_1^2 + \varphi_2^2 - \varphi_1\varphi_2 - \varphi_0^2)/3 + \Delta \tag{A.22}$$

and

$$u = L(\varphi_1^2 + \varphi_2^2 + \varphi_1\varphi_2 - 3\varphi_0^2)/3 + \Delta \tag{A.23}$$

for the shapes in Fig. 4(b) and (c), respectively.

If we further assume that not only the initial imperfections are represented by equal angles but the models deform in a way that the rotational angles remain equal, then the corresponding expressions for the vertical displacements become

$$u = L(\varphi^2 - \varphi_0^2)/3 + \Delta \tag{A.24}$$

and

$$u = L(\varphi^2 - \varphi_0^2) + \Delta. \tag{A.25}$$

for the models in Fig. 4(b) and (c), respectively.

Appendix B. Progressive buckling

B.1. Equation of motion

The circumferential forces $F^{\theta}(x)$ in a circular cylindrical shell that buckles axisymmetrically give rise to components $F^{c}(x) = F^{\theta}(x)/R$ when projected in the direction perpendicular to the mid surface and these components contribute to the bending moments. The forces $F^{c}(x)$ account for the bi-axial stress state that is characteristic of the bending phase and should be added to the bending moments of the model as shown in Fig. 16

$$M_c(t) = \int_0^l F^c(x,t)x\cos\phi\,dx. \tag{B.1}$$

However, the circumferential forces are determined only for the cells of the model due to the discrete approach used, so that an appropriate distribution of F^c has to be assumed along the rigid links in order

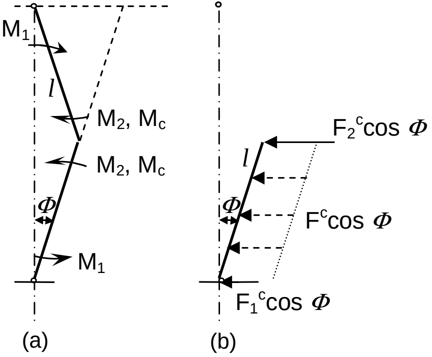

Fig. 16. (a) The hinge mechanism for the buckling phase, (b) bending moment due to the circumferential forces.

to obtain a more realistic estimation of the influence of the circumferential forces. An average value $F^{c}(x,t) = (F_1^{c}(t) + F_2^{c}(t))/2 = F^{c}(t)$ is assumed in the present analysis as shown in Fig. 16(b) and as assumed by Karagiozova and Jones (2000). Therefore, $M_c(t)$ approximates the bending moment due to the circumferential forces in a shell and is determined as

$$M_c(t) = \frac{1}{2}F^{c}(t)l^2\cos\phi. \tag{B.2}$$

By taking angle ϕ as a generalized coordinate, the kinetic energy of the model in Fig. 16(a) is

$$T = \frac{2}{3}ml^2\dot{\phi}^2 + 2l^2(m^* + G)\sin^2\phi\phi^2. \tag{B.3}$$

If a virtual displacement $\mathrm{d}\phi$ is given to the system, then the virtual work done by the active forces is

$$-2M_1\delta\phi - 2M_2\delta\phi - 2M_c\delta\phi, \tag{B.4}$$

so that the generalized force corresponding to the generalized coordinate ϕ is

$$Q_\phi = -2M_1 - 2M_2 - 2M_c. \tag{B.5}$$

The equation of motion of the model is obtained from Lagrange's equation

$$\frac{\mathrm{d}}{\mathrm{d}t}\left(\frac{\partial T}{\partial\dot{\phi}}\right) - \frac{\partial T}{\partial\phi} = Q_\phi. \tag{B.6}$$

as

$$\ddot{\phi} = -\frac{2l^2(m^* + G_1)\dot{\phi}^2\sin\phi\cos\phi + M_1(t) + M_2(t) + 0.5F^{c}(t)l^2\cos\phi}{2l^2[m^*/3 + (m^* + G_1)\sin^2\phi]}, \tag{B.7}$$

when substituting Eqs. (B.3) and (B.5) into Eq. (B.6).

B.2. Stress–strain relationships for elastic–plastic media subjected to a plane stress state and conforming to the Tresca yield criterion

It is assumed that the strain increments are divided into elastic and plastic parts, so that the total increments are

$$\begin{aligned} \mathrm{d}\varepsilon_x &= \mathrm{d}\varepsilon_x^{\mathrm{p}} + (\mathrm{d}\sigma_x - v\mathrm{d}\sigma_\theta)/E, \\ \mathrm{d}\varepsilon_\theta &= \mathrm{d}\varepsilon_\theta^{\mathrm{p}} + (\mathrm{d}\sigma_\theta - v\mathrm{d}\sigma_x)/E, \\ \mathrm{d}\varepsilon_z^{\mathrm{p}} &= -(\mathrm{d}\varepsilon_x^{\mathrm{p}} + \varepsilon_\theta^{\mathrm{p}}), \end{aligned} \tag{B.8}$$

where v is the Poisson ratio. The equivalent stress increment, $\mathrm{d}\sigma_e$, satisfies the relation $\mathrm{d}\sigma_e = H'\mathrm{d}\varepsilon_p$, $H' = E\lambda/(1-\lambda)$, where ε_p is the equivalent plastic strain. The increment of the equivalent stress for the Tresca yield criterion in terms of the principal stresses is

$$\mathrm{d}\sigma_e = \mathrm{d}\sigma_1 - \mathrm{d}\sigma_2, \tag{B.9}$$

where σ_1 and σ_2 are the minimum and maximum principal stresses. Neglecting the shear stress, the flow rules for a material with a linear strain hardening can be obtained as

$$\mathrm{d}\varepsilon_x^{\mathrm{p}} = \frac{\sqrt{3}}{2H'}\mathrm{d}\sigma_x, \quad \mathrm{d}\varepsilon_\theta^{\mathrm{p}} = 0, \quad \mathrm{d}\varepsilon_z^{\mathrm{p}} = -\mathrm{d}\varepsilon_x^{\mathrm{p}} \tag{B.10}$$

for $\mathrm{d}\sigma_\mathrm{e} = |\mathrm{d}\sigma_x|$,

$$\mathrm{d}\varepsilon_x^\mathrm{p} = 0, \quad \mathrm{d}\varepsilon_\theta^\mathrm{p} = \frac{\sqrt{3}}{2H'}\mathrm{d}\sigma_\theta, \quad \mathrm{d}\varepsilon_z^\mathrm{p} = -\mathrm{d}\varepsilon_\theta^\mathrm{p} \tag{B.11}$$

for $\mathrm{d}\sigma_\mathrm{e} = |\mathrm{d}\sigma_\theta|$ and

$$\mathrm{d}\varepsilon_x^\mathrm{p} = -\frac{\sqrt{3}}{2H'}(\mathrm{d}\sigma_x - \mathrm{d}\sigma_\theta), \quad \mathrm{d}\varepsilon_\theta^\mathrm{p} = -\mathrm{d}\varepsilon_x, \quad \mathrm{d}\varepsilon_z^\mathrm{p} = 0 \tag{B.12}$$

for $\mathrm{d}\sigma_\mathrm{e} = |\mathrm{d}\sigma_\theta - \mathrm{d}\sigma_x|$.

The stress increments associated with each side of the Tresca hexagon are obtained when substituting the corresponding Eqs. (B.10), (B.11) or (B.12) into Eqs. (B.8).

$$\begin{aligned} \mathrm{d}\sigma_x &= 2\lambda E(\mathrm{d}\varepsilon_x + v\,\mathrm{d}\varepsilon_\theta)[(1-\lambda)\sqrt{3} + 2\lambda(1-v^2)]^{-1}, \\ \mathrm{d}\sigma_\theta &= E\{2\lambda v\,\mathrm{d}\varepsilon_x + [(1-\lambda)\sqrt{3} + 2\lambda]\,\mathrm{d}\varepsilon_\theta\}[(1-\lambda)\sqrt{3} + 2\lambda(1-v^2)]^{-1} \end{aligned} \tag{B.13}$$

for those sides with $\mathrm{d}\sigma_\mathrm{e} = |\mathrm{d}\sigma_x|$.

$$\begin{aligned} \mathrm{d}\sigma_x &= E\{[(1-\lambda)\sqrt{3} + 2\lambda]\mathrm{d}\varepsilon_x + 2\lambda v\,\mathrm{d}\varepsilon_\theta\}[(1-\lambda)\sqrt{3} + 2\lambda(1-v^2)]^{-1}, \\ \mathrm{d}\sigma_\theta &= 2\lambda E(v\,\mathrm{d}\varepsilon_x + \mathrm{d}\varepsilon_\theta)[(1-\lambda)\sqrt{3} + 2\lambda(1-v^2)]^{-1} \end{aligned} \tag{B.14}$$

for the sides of the Tresca hexagon with $\mathrm{d}\sigma_\mathrm{e} = |\mathrm{d}\sigma_\theta|$ and

$$\begin{aligned} \mathrm{d}\sigma_x &= \frac{E}{2(1-v)[(1-\lambda)\sqrt{3} + \lambda(1+v)]}\{[(1-\lambda)\sqrt{3} + 2\lambda]\,\mathrm{d}\varepsilon_x + [(1-\lambda)\sqrt{3} + 2\lambda v]\,\mathrm{d}\varepsilon_\theta\}, \\ \mathrm{d}\sigma_\theta &= \frac{E}{2(1-v)[(1-\lambda)\sqrt{3} + \lambda(1+v)]}\{[(1-\lambda)\sqrt{3} + 2\lambda v]\,\mathrm{d}\varepsilon_x + [(1-\lambda)\sqrt{3} + 2\lambda]\,\mathrm{d}\varepsilon_\theta\} \end{aligned} \tag{B.15}$$

for the sides with $\mathrm{d}\sigma_\mathrm{e} = |\mathrm{d}\sigma_x - \mathrm{d}\sigma_\theta|$.

References

Abramowicz, W., Jones, N., 1997. Transition from initial global bending to progressive buckling of tubes loaded statically and dynamically. International Journal of Impact Engineering 19 (5–6), 415–437.

Alexander, J.M., 1969. An approximate analysis of the collapse of thin cylindrical shells under axial load. Quarterly Journal of Mechanics and Applied Mathematics 13, 10–15.

Alves, M., 2000. Material constitutive law for large strains and strain rates. Journal Engineering Mechanics 126 (2), 215–218.

Andrews, K.R.F., England, G.L., Ghani, E., 1983. Classification of the axial collapse of circular tubes under quasi-static loading. International Journal of Mechanical Sciences 25, 687–696.

Jones, N., 1974. Some remarks on the strain-rate sensitive behaviour of shels. In: Sawczuk, A. (Ed.), Problems of Plasticity, vol. 2. Noordhoff, Groningen, pp. 403–407.

Jones, N., 1989. Structural Impact. Cambridge University Press, Cambridge.

Karagiozova, D., Alves, M., Jones, N., 2000. Inertia effects in axisymmetrically deformed cylindrical shells under axial impact. International Journal of Impact Engineering 24 (10), 1083–1115.

Karagiozova, D., Jones, N., 2000. Dynamic elastic–plastic buckling of circular cylindrical shells under axial impact. International Journal of Solids and Structures 37, 2005–2034.

Karagiozova, D., Jones, N., 2001. Influence of stress waves on the dynamic progressive and dynamic plastic buckling of cylindrical shells. International Journal of Solids and Structures 38, 6723–6749.

Karagiozova, D., Jones, N., 2002. On dynamic buckling phenomena in axially loaded elastic–plastic cylindrical shells. International Journal of Non-Linear Mechanics 37, 1223–1238.

Karagiozova, D., Alves, M., 2004. Transition from progressive buckling to global bending of circular shells under axial impact—Part I: Experimental and numerical observations. International Journal of Solids and Structures 41, 1565–1580.

Su, X.Y., Yu, T.X., Reid, S.R., 1995. Inertia-sensitive impact energy absorbing systems, Part I– Effect of inertia and elasticity. International Journal of Impact Engineering 16, 561–672.

Tam, L.L., Calladine, C.R., 1991. Inertia and strain-rate effects in a simple plate-structure under impact loading. International Journal of Impact Engineering 11, 349–377.

Wierzbicki, T., Sinmao, M.V., 1997. A simplified model of Brazier effect in plastic bending of cylindrical tubes. International Journal of Pressure Vessels 71 (1), 19–28.

Zhang, T.G., Yu, T.X., 1989. A note on a 'velocity sensitive' energy-absorbing structure. International Journal of Impact Engineering 8 (1), 43–51.